Field-scale sugarcane mapping in Thailand by fusing annual satellite embeddings with a global field-boundary model, cross-checked against mill weighbridge records

Watcharapon Thod

Department of Computer Science, Faculty of Science, Kasetsart University, Bangkok, Thailand

Correspondence: pisit.leephathr@gmail.com

Abstract

Sugarcane in Thailand is grown almost entirely by smallholders who deliver to mills under seasonal contracts, so the quantities that matter to planning are properties of individual fields rather than of pixels. Published Thai cane maps are per-pixel classifications, and global cane products perform markedly worse in Thailand than elsewhere because cane is confused with cassava. Whether the global field-delineation models released in the past two years can supply the missing parcel geometry for Thai smallholder cane has not been tested. We combined the AlphaEarth Satellite Embedding dataset with the Fields of The World (FTW) global boundary product to build a field-scale cane parcel map over a mill catchment of about 8,300 km² in central Thailand, and cross-checked it against 74,516 weighbridge delivery tickets covering 1.54 million tonnes from 8,924 known fields. Cane was classified per pixel from three years of 64-band annual embeddings using two-step positive-unlabelled learning (Liu et al., 2002; Elkan & Noto, 2008; Bekker & Davis, 2020); parcels were taken from FTW and labelled as cane when at least half of their area fell inside the predicted mask. The detector recalled 93.2% of held-out registered cane pixels at a 5.3% false-positive rate and fired on 97.0% of 1,500 fields already carrying cane before they entered the registry. The fused layer resolved 67,251 parcels of median size 8.0 rai against 0.6 rai for raw FTW parcels; 59.4% showed a harvest-scale NDVI collapse in both milling seasons. Visual interpretation of paired seasonal imagery over the 299 highest-ranked unregistered parcels returned a precision of 0.946 (95% CI 0.915–0.967); a stratified assessment of the full layer is in progress and no map-level accuracy is claimed until it is complete.

Highlights

- A global field-boundary product over-fragments Thai smallholder cane fields by a factor of about twenty (median 0.6 rai against 14.8 rai for contract fields).
- Fusing annual satellite embeddings with borrowed parcel geometry yields 67,251 field-scale cane parcels over an 8,300 km² mill catchment.
- Detection is cross-checked against 74,516 weighbridge tickets, reference data that image-based crop studies rarely have.
- An oracle-mask diagnostic shows the residual error is in the cane mask, not in the parcel decoder.
- At 10 m, sub-pixel boundary accuracy would be needed to reach IoU 0.8 on fields of 0.5–1.6 ha, which bounds what any model can achieve in this setting.

Keywords: sugarcane; field boundaries; satellite embeddings; Sentinel-2; positive-unlabelled learning; Thailand

Contents

List of Figures

List of Tables

1. Introduction

Field-scale crop maps support supply-chain forecasting, harvest logistics, and policy compliance, and sugarcane in Thailand is a case where the field, not the pixel, is the unit of every decision. Mills contract with individual growers, issue quotas per field, dispatch harvest crews per field, and pay per delivery on a sugar content (CCS) basis, so a map that reports “cane here” without saying “this field, this many rai” cannot be acted upon. The same granularity has become a policy requirement: burnt-cane penalties, zero-burning programmes, and ratoon-age management are all administered per field.

Three layers of the mapping problem are unresolved, and they are unresolved in a specific order. First, sugarcane maps for Thailand already exist and are accurate at the pixel level — regional classifications report overall accuracies above 95% (Suwanlee et al., 2025) and national mapping with deep networks on high-resolution imagery has been demonstrated (Poortinga et al., 2021) — but they deliver rasters, not parcels, and a raster cannot be joined to a delivery ticket. Second, where cane has been mapped globally rather than regionally, Thailand is the country where the approach breaks down: Di Tommaso et al. (2024) report F1 scores above 0.9 for several major producers but 0.57 for Thailand, attributed to confusion with cassava. Our own registry data show why that confusion is structural rather than incidental: among 35,979 field-seasons with a recorded preceding crop, 86.7% followed cane, 3.8% followed cassava and 3.8% followed maize, so cassava is not a distant neighbour in the landscape but the crop that alternates with cane on the same parcels. Third, the two model families that could in principle supply the missing pieces have not been brought to this crop. Global field-boundary segmentation has advanced quickly with the release of the Fields of The World benchmark and models (Kerner et al., 2024), but has not been evaluated against Thai smallholder cane; and geospatial foundation models that compress a year of multi-sensor observations into a per-pixel embedding — of which AlphaEarth (Brown et al., 2025) is the first with global, freely available annual coverage at 10 m — have been applied to irrigation mapping, US crop-type benchmarks and specialty crops, but not to sugarcane and not in Thailand.

To fill this gap we treat the problem as a fusion rather than a classification task. An embedding-based classifier is used for what it does well — deciding whether a pixel is cane, using ratoon persistence across years as the discriminating signal — and a global boundary model is used for what a per-pixel classifier cannot do, namely cutting a continuous cane region into parcels. The mill registry, which records the polygon, the season, and the grower of every contracted field, provides labels; the mill weighbridge, which records every truckload delivered, provides a form of ground truth that satellite studies rarely have, because it is a physical measurement of harvested biomass rather than an interpretation of an image.

We deliberately do not frame the product as a detector of illicit cultivation. The catchment straddles provinces served by other mills, so a field's absence from this registry is uninformative about its legal status; the registry comparison is reported at the end as one application of the map, with that ambiguity measured rather than assumed.

The contributions are: (i) the first application of AlphaEarth annual embeddings to sugarcane, and a field-scale cane parcel layer for a Thai mill catchment built by fusing them with a global boundary product; (ii) the first quantitative evaluation of FTW boundaries against a large operational registry of smallholder cane fields, which shows a strong over-fragmentation bias (median FTW parcel 0.6 rai against a median registered field of 14.8 rai across all 44,469 registry polygons) and a coverage that varies by a factor of two between vintages; (iii) an out-of-sample detection check built from the registry's own history — 1,500 fields whose land carried cane before they were registered — that avoids the circularity of measuring a discovery system on the labels it was trained on; (iv) a diagnosis of where the remaining error lives, obtained by feeding the decoder an oracle mask, which moves isolated-field IoU from 0.61 to 1.00 and shows that the bottleneck is the cane mask rather than the instance decoder; and (v) two negative results reported in full — a geotagged-photograph evidence channel that a displacement null model shows to be anti-correlated with the target, and a purpose-trained delineation model that does not reach its pre-declared targets; and (vi) a pipeline whose four inputs are all free and public, so that the method transfers to any catchment where a local reference set can be assembled, even though the reference records used here are confidential and are not released.

2. Study area and data

2.1 Study area

The study area is the cane catchment of one mill group in the transition between Thailand's upper central plain and the western edge of the Khorat plateau. Mapped cane parcels lie between 14.81° and 16.27° N and between 100.53° and 102.00° E; the footprint, defined as the union of 1 km grid cells containing at least one mapped cane parcel, covers 8,295 km², of which the cells containing at least one registered field cover 3,694 km². The mill divides the catchment into 22 extension zones, which are used throughout as spatial blocking units for train/test splits. Assigning each registered field to a province through the administrative code of its nearest FTW parcel places 76.2% of registrations in Phetchabun, 16.7% in Lop Buri, 3.8% in Chaiyaphum, 1.8% in Nakhon Sawan and 1.5% in Nakhon Ratchasima, with seven fields in Saraburi and Phichit. This distribution matters for interpretation as much as for description: five provinces are involved, other mills operate in all of them, and there is no national parcel registry that would allow a field to be traced to its buyer.

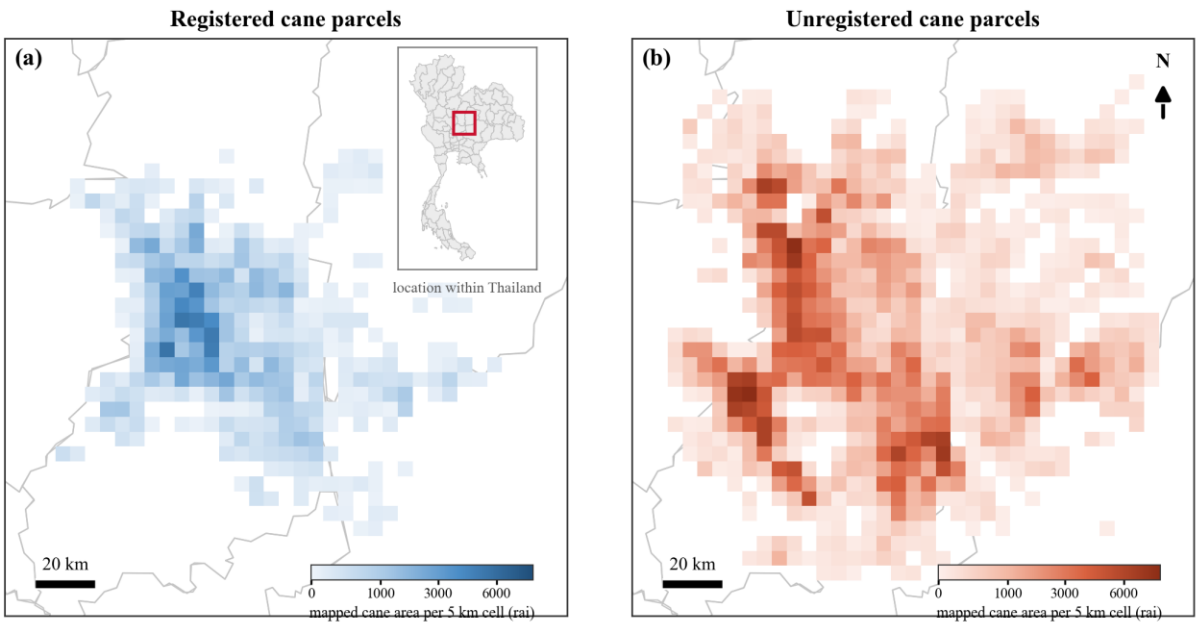

Grey lines are province boundaries, shown unlabelled. Cell values are total mapped cane area per 5 km cell;
no individual parcel geometry, coordinate axis or place name below province level is shown.

Figure 1. Study area. Density of mapped cane, aggregated to a 5 km grid, over the five provinces of the mill catchment; province boundaries and a scale bar are shown, individual parcels are not. Registered and unregistered components are shown as two panels of the same grid. Inset: location within Thailand. Cell values are areas per cell; no parcel geometry, coordinate list or place name below province level is published.

Areas are reported in rai, the operational unit of Thai agriculture (1 rai = 1,600 m² = 0.16 ha), with hectare equivalents at first use. Seasons follow the mill's Thai crop-year labels, abbreviated 66 to 69; season 68 is used most often below and its cane was delivered between 9 January and 4 April 2026.

2.2 Registered field polygons

Registered field polygons for seasons 66–69 comprise 44,469 field-seasons (10,929 / 10,129 / 11,094 / 12,317 for seasons 66 / 67 / 68 / 69), each carrying a contract polygon, a grower identifier, a season, and a declared preceding crop. The polygons are contract geometry: they delimit what a grower committed to deliver, not necessarily what is physically visible as one field. A structural consequence recurs throughout this paper — several registrations frequently subdivide one uninterrupted block of cane, and no image-based model can recover that subdivision.

2.3 Weighbridge delivery records

Weighbridge (truck-scale) delivery records for season 68 comprise 74,516 deliveries from 8,924 registered fields, totalling 1,542,045 t of cane, with a laboratory CCS value per delivery (mean 12.93, range 9.47–15.87 across fields). Deliveries were recorded between 9 January and 4 April 2026. Because the weighbridge sees only cane that arrived at this mill, it provides one-sided evidence: a delivery proves that the field grew and cut cane, while the absence of a delivery is ambiguous. That asymmetry is used explicitly in Section 4.1. Cross-referencing the two tables shows that 2,170 of 11,094 season-68 registrations (19.6%) produced no delivery at all.

2.4 Field evaluations and geotagged photographs

Field-evaluation records for season 69 cover 7,039 fields and carry 29,376 geotagged photographs taken by mill extension officers. Because one visit typically uploads about three images at an identical coordinate, the photographs correspond to 10,178 distinct coordinates and 9,375 distinct evaluations, and all counts below are reported at all three levels. These records were tested as an independent evidence channel; Section 4.8 reports why they cannot serve that purpose.

2.5 AlphaEarth annual embeddings

Input features were taken from the public AlphaEarth Satellite Embedding dataset, which provides annual 64-band images at 10 m spatial resolution (produced by Google and Google DeepMind, CC-BY 4.0), for the years 2023, 2024 and 2025 over UTM zone 47N. Tiles were read directly from cloud-optimized GeoTIFFs by range request; no imagery was stored locally.

2.6 Sentinel-2 L2A

Monthly Sentinel-2 L2A composites were used for the harvest-cycle evidence layer, covering the November–April milling window of two consecutive seasons. Scenes were retrieved from the AWS Earth Search STAC catalogue with the Microsoft Planetary Computer as a fallback; a monthly value is the median of up to a fixed number of cloud-sorted accepted scenes. Reflectance offsets were applied only when they survived a negative-reflectance guard, because the two catalogues differ in whether the offset has already been applied to the stored digital numbers.

2.7 Fields of The World global boundaries

Field boundaries were taken from the Fields of The World global predictions for Thailand (CC-BY), read by HTTP range request from the public parquet distribution. Two annual vintages are present in the source file, labelled 2567 and 2568 in the Thai calendar (2024 and 2025). The subset covering the study area contains 4,396,674 polygons — 2,562,127 for 2567 and 1,834,547 for 2568 — with a median polygon area of 0.60 rai (2567) and 1.14 rai (2568) and a total delineated area of 10,022 km² and 12,050 km² respectively.

2.8 ESA WorldCover

ESA WorldCover 2021 v200 (10 m, CC-BY) was used as an independent, fully public cross-check of the fused layer. It separates cropland from water, built-up land, forest and grassland but cannot distinguish sugarcane from cassava, so it bounds gross commission error without estimating precision.

2.9 Confidentiality

The three reference datasets — registered field polygons, weighbridge delivery and CCS records, and field-evaluation photographs — are commercially confidential property of the mill group and are used here under agreement. All grower-identifying attributes were removed before analysis, no per-parcel coordinate, field identifier, grower identifier or quota code appears anywhere in this paper or its supplementary material, and every result is reported as an aggregate statistic or as a deliberately generalized map product, in compliance with Thailand's Personal Data Protection Act (PDPA). Place names are given no finer than province level. The four input datasets used to produce the map itself (Sections 2.5–2.8) are all public.

Table 1. Data sources and summary statistics.

Source	Period	Volume	Role in this study
Registered field polygons	seasons 66–69	44,469 field-seasons (10,929 / 10,129 / 11,094 / 12,317)	positive labels; boundary reference; registry comparison
Weighbridge delivery records	season 68 (9 Jan – 4 Apr 2026)	74,516 deliveries, 8,924 fields, 1,542,045 t, CCS 9.47–15.87	delivery-verified labels; ambiguity analysis
Field evaluations with photographs	season 69 (Jul–Aug 2026)	29,376 photos / 10,178 coordinates / 9,375 evaluations / 7,039 fields	tested evidence channel (negative result)
AlphaEarth Satellite Embedding	2023, 2024, 2025	64 bands, 10 m, annual	classification features
Sentinel-2 L2A	Nov–Apr, two seasons	monthly median composites	harvest-cycle evidence
Fields of The World (Thailand)	vintages 2567, 2568	4,396,674 polygons in study area	parcel geometry; external boundary baseline
ESA WorldCover v200	2021	10 m global land cover	independent public cross-check

The first three rows are confidential mill records used under agreement; the last four are public datasets, so the method is reproducible anywhere without them (Data and code availability).

3. Methods

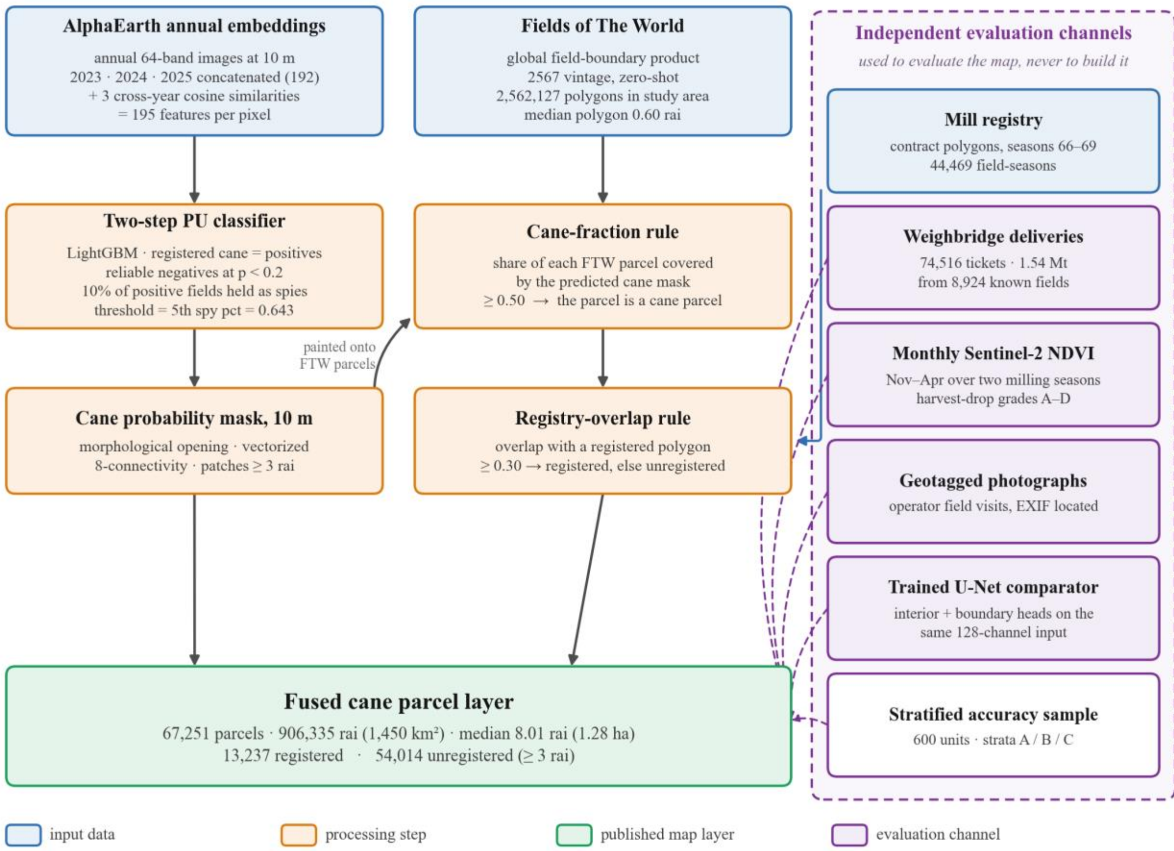

Figure 2. Method overview. Three years of AlphaEarth annual embeddings feed a two-step positive-unlabelled classifier calibrated with spies; the resulting cane mask is painted onto Fields of The World parcels; parcels covered at least 50% by cane become cane parcels and are labelled registered or unregistered by a 30% overlap rule with the mill registry. Independent checks — weighbridge deliveries, monthly Sentinel-2 NDVI, geotagged photographs and a trained delineation model — are shown as separate inputs to evaluation rather than to the map.

3.1 Pixel-level sugarcane classification from annual embeddings

For each 10 m pixel, embeddings from 2023, 2024 and 2025 were concatenated (192 dimensions) and augmented with three cross-year cosine similarities (2023–24, 2024–25, 2023–25), yielding 195 features. The similarity features were motivated by ratoon persistence: cane kept as ratoon for three or four seasons exhibits a stable cross-year signature, whereas annually rotated crops do not, and 86.7% of field-seasons with a known preceding crop followed cane.

Because the registry records where cane is but never where it is not, the classifier was trained under a positive-unlabelled formulation. Registered-cane pixels supplied positives and pixels more than 200 m from any registration supplied unlabeled negatives for a first LightGBM (Ke et al., 2017) stage; reliable negatives were then selected where the first-stage probability fell below 0.2, and a second classifier was trained on positives against reliable negatives. Ten percent of positive fields were withheld as spies and the decision threshold was set at the fifth percentile of spy probabilities, clipped to [0.5, 0.9], which yielded 0.643. Train and test negatives were drawn disjointly and the holdout was stratified by extension zone so that no zone contributed to both fitting and evaluation.

At inference, a 150-tree gate model on current-year embeddings (threshold 0.15) filtered pixels before full-model scoring, which allowed streaming inference over the catchment directly from cloud-optimized GeoTIFFs. Predicted masks were cleaned by morphological opening, vectorized with 8-connectivity, and filtered to patches of at least 3 rai. Patch boundaries were regularized by guarded simplification: a 10 m tolerance was accepted only when the simplified polygon retained IoU ≥ 0.93 and an area change $\leq 3\%$ against the raw patch, falling back to 5 m or to the raw boundary otherwise.

3.2 Parcel geometry from Fields of The World

Field boundaries were taken from FTW without retraining or fine-tuning, so that the comparison in Section 4.2 measures the product as a user would obtain it. Polygons were filtered to the study-area bounding box and to one vintage at a time. For the external benchmark, each registered polygon was matched to every intersecting FTW polygon and two agreement measures were computed: a best-match IoU, defined as the maximum IoU over intersecting polygons, and a union IoU, in which all FTW polygons lying more than half inside the registered field were merged before scoring. The union measure is the fairer one for an over-fragmenting predictor, because it credits a model that draws the right outer boundary but adds internal cuts. The number of such interior polygons per field was recorded as a fragmentation count, and fields with no intersecting FTW polygon at all were counted separately as coverage failures. All benchmark geometry was reprojected to UTM 47N and fields smaller than 800 m^2 were dropped.

3.3 Fusion into a field-scale cane layer

The fused layer was constructed by painting the pixel-level cane prediction onto FTW parcel geometry. For every FTW polygon, the fraction of its area covered by the predicted cane mask was computed, and polygons with a cane fraction of at least 0.5 were labelled as cane parcels. Each cane parcel was then intersected with the registry, and a parcel whose area overlapped registered polygons by at least 0.3 was marked as registered and otherwise as unregistered. Parcels smaller than 3 rai were excluded from the reported unregistered set, matching the minimum patch size of the detector. All overlap computations were carried out in geographic coordinates using area ratios, in which the local scale factor cancels, which avoided reprojecting several million polygons; areas were converted to rai using the metric scale at the study-area latitude.

The two thresholds are the only free parameters of the fusion and both were fixed a priori rather than tuned against any evaluation set: 0.5 expresses “more cane than not” and 0.3 expresses “materially overlapping an existing contract”.

3.4 Harvest-cycle evidence from monthly Sentinel-2 NDVI

Sugarcane is cut inside the milling window, so a genuine cane parcel must show a large NDVI collapse somewhere between November and April, whereas a parcel that never greens or never drops is a false-positive suspect. Monthly NDVI was therefore computed for every candidate parcel over two consecutive milling seasons, with zonal means taken by binned counting on a rasterized label image so that one windowed read served every parcel inside a spatial block. A harvest event was flagged when the largest month-to-month drop reached 0.15, measured relative to the seasonal peak, and each parcel was assigned one of two failure classes when no drop was found: never green, or green but never dropping.

Parcels were then graded by combining the channels, which are independent in the sense that they use different sensors, different temporal resolutions and different physical signals: grade A when a harvest drop was detected in both seasons, B when it was detected in one, C when the parcel stayed evergreen across both, D when it never greened, and E when a photograph independently indicated that the parcel is in fact registered land (Section 3.6).

3.5 A trained boundary model as an internal comparator

To establish whether a purpose-trained model would outperform the global product on this landscape, detection and delineation were also trained jointly. A U-Net (Ronneberger et al., 2015) of 4.07 M parameters was trained on 128 × 128 pixel windows (1.28 km on a side) carrying the AlphaEarth embeddings of two consecutive years (128 input channels), and three outputs were predicted per pixel: a cane interior probability, a normalized distance-to-boundary map, and a parcel-boundary probability. Registered polygons of seasons 67–69 supplied the supervision and the loss was applied over the entire window rather than over parcel cores only. Instances were decoded in three ways from the same forward pass, referred to below as arms: connected components of the thresholded interior mask; a marker-controlled watershed (Beucher & Meyer, 1993) seeded by the distance map; and the same watershed with the predicted boundary probability added as a barrier. The three thresholds (interior 0.4, marker 0.35, boundary 0.6) were selected by a sweep on a selection split drawn from four extension zones that were disjoint from both the fitting and the holdout zones. Each registered polygon inside the holdout windows was rasterized on the 10 m grid and its IoU against the decoded instance was computed; fields touching a window border were excluded, as were fields below a minimum pixel count. Two targets were declared before training: a median IoU of 0.85 on isolated fields and 60% of adjacent fields separated at IoU $\geq$ 0.8.

Five configurations were run and are reported as an ablation in Section 4.5. Between loop-1 and loop-3 the input was extended from one year of embeddings to two, the loss was extended from parcel cores (13.8% of pixels) to the full window, and 10,481 season-69 polygons whose stored rings were not closed were repaired and added to the label set. Loop-4a added dropout and dual-GPU training; loop-5 added a Dice term on the interior head, early stopping with patience 15, and a larger window pool (raised from 2,000 to 5,000 windows per season, capped at 9,500 by host memory), and was evaluated on a different holdout.

The embedding year was mapped to the season as 67 → 2023, 68 → 2024 and 69 → 2025, with the preceding year supplying the second input; because AlphaEarth annual embeddings were published only through 2025 at the time of analysis, the most recent registrations could not be paired with imagery from their own growth year. The consequences are discussed in Section 6.

3.6 A zero-shot segmentation baseline

Before the comparator of Section 3.5 was trained, a prompt-driven zero-shot segmentation model (Segment Anything; Kirillov et al., 2023) was applied to the same holdout blocks as an external reference point. Interior points of each detected cane component were used as positive prompts, a returned mask was accepted when the detected component was contained within it, and the resulting instances were scored against registry polygons with the intersection-over-union protocol used elsewhere in this paper. This baseline is reported only as a reference level for what an off-the-shelf segmentation model achieves on this imagery without any training on cane; it forms no part of the production layer.

3.7 Evaluation protocols

Four protocols were used, each designed to remove a specific form of circularity.

Held-out zones. Detection recall was measured on registered fields in extension zones that contributed no training pixels, and the false-positive rate on disjoint far-negative samples.

Out-of-sample detection. Because recall measured on registered fields is circular for a system whose purpose is to find fields outside the registry, two sets that had never been used for training were drawn from the registry's own history. The positive set comprised 1,500 fields first registered in season 69 whose land had already carried cane in the preceding season — cane that was physically present and administratively invisible at image time. The negative-proxy set comprised 800 season-68 registrations that delivered no cane at the weighbridge, of which 797 could be scored. The detector was applied at its calibrated threshold of 0.643 and the detected fraction and median predicted probability were recorded for each set.

Registry-reveal protocol. Registered polygons are available at inference time and can be used as fixed walls when cutting a block of cane into parcels, but scoring a model on fields whose boundaries it was given is leakage. A reveal protocol was therefore used: within each window a random fraction r of fields was revealed — their area removed from the mask and their boundary imposed as a wall — and accuracy was measured only on the fields that stayed hidden. Two rates were run, $r = 0.5$ and $r = 0.76$, the latter being the observed fraction of adjacent cases that touch at least one registered field. Revealed fields were removed by area only, without eroding neighbours, so that hidden fields were not artificially trimmed.

Oracle diagnostics. To locate the residual error, the decoder was rerun with components replaced one at a time: the predicted interior mask replaced by the rasterized ground-truth mask (oracle mask); the interior threshold replaced by the per-field best choice from a sweep (oracle threshold); and the decoded instance dilated or eroded by one pixel. The gap that each substitution closes identifies the component that limits the result.

Null model for the photograph channel. Every photograph coordinate was displaced by a random 0.5–2 km and the spatial join was repeated, six replicates at the 50 m buffer and eight for the strict rule, giving the hit count expected if photograph positions carried no information about parcel locations.

3.8 Independent cross-check against a public land-cover product

Because every check described so far uses confidential mill records, one check was built entirely from public data so that it can be repeated by anyone. A random sample of 1,500 fused cane parcels of at least 3 rai was drawn with a fixed seed, each parcel was rasterized onto the ESA WorldCover 10 m grid, and the dominant land cover class inside the parcel was recorded together with the cropland fraction. Parcels whose dominant class was built-up, water or tree cover were counted as gross commission errors, since no sugarcane field can be any of those. The test was declared in advance to be a bound on gross error and not an estimate of precision, because WorldCover assigns sugarcane and cassava to the same cropland class.

3.9 Design of the stratified accuracy assessment

Map accuracy is being estimated by stratified random sampling following Olofsson et al. (2014). Three strata were defined over the fused layer: parcels mapped as cane and not registered (A), parcels mapped as cane and registered (B), and locations the map assigns to no cane parcel (C). Sample sizes of 250, 100 and 250 were drawn with a fixed seed, giving 600 sample units;

stratum C points were rejected unless they fell more than about 100 m from any mapped cane parcel, and each is presented to the interpreter as a 120 m context box. Inclusion probabilities were stored with every unit so that unbiased area estimation is possible, and units were shuffled before presentation so that the interpreter cannot infer a unit's stratum from its position in the queue. Interpretation is against sub-metre basemap imagery with a three-way verdict (cane / not cane / unsure); unsure verdicts are reported separately rather than being redistributed. From the completed verdicts, user's and producer's accuracies, overall accuracy weighted by stratum area, Cohen's kappa, Wilson confidence intervals, and an unbiased cane-area estimate will be computed. The design and the scoring code were fixed before any label was collected.

4. Results

4.1 Pixel-level detection and out-of-sample checks

The spy-calibrated threshold was 0.643. On registered fields in held-out extension zones the detector recalled 93.2% of cane pixels, and on disjoint far-negative samples the false-positive rate was 5.3%. Applied to the catchment, the detector returned 23,550 patches of at least 3 rai covering 1,241,386 rai across 22 extension zones, with zone totals from 6,906 to 204,782 rai. The out-of-sample checks are more informative than the held-out recall. On the 1,500 fields that carried cane before they were registered, 97.0% were detected at the operating threshold (1,455/1,500; 95% Wilson CI 96.0–97.8), with a median predicted probability of 0.9951 — that is, the detector finds cane that the registry did not yet know about, on fields it never saw in training. On the 797 season-68 registrations that delivered no cane, 89.6% were also detected (714/797; CI 87.3–91.5), with a median probability of 0.991. Two readings of that second number are consistent with the data: the detector false-positives on this population, or the land still grows cane whose harvest is delivered elsewhere. They cannot be separated with a single mill's weighbridge, because a delivery to another mill leaves no trace in these records. Both readings have consequences — the first bounds achievable precision, the second means that non-delivering registrations must never be reused as negative labels — and the 19.6% of season-68 registrations that delivered nothing is therefore treated as an ambiguous, not a negative, class.

Table 2. Pixel-level sugarcane detection and out-of-sample checks. Wilson 95% confidence intervals; n is fields except where noted.

Quantity	Value	n	95% CI
Spy-calibrated decision threshold	0.643	—	—
Recall, held-out extension zones (pixels)	93.2%	pixel-level	—
False-positive rate, far negatives (pixels)	5.3%	pixel-level	—
Detected patches ≥ 3 rai	23,550 patches / 1,241,386 rai	—	—
Detection on cane present before registration	97.0% (1,455)	1,500	96.0–97.8
Median probability, same set	0.9951	1,500	—
Detection on non-delivering registrations	89.6% (714)	797	87.3–91.5
Median probability, same set	0.991	797	—
Season-68 registrations with no delivery	19.6% (2,170)	11,094	18.8–20.3

4.2 Global field boundaries against the mill registry

FTW boundaries were scored against registered fields for the two vintages present in the source file (Table 3). Against season 68, FTW 2567 reached a median best-match IoU of 0.398 and a median union IoU of 0.493, with 9.3% of fields reaching union IoU ≥ 0.8 and 30.9% of fields having no intersecting FTW polygon at all. Against season 69, FTW 2568 reached a median best-match IoU of 0.297 and a median union IoU of 0.295, with 9.5% at union IoU ≥ 0.8 and 59.4% of fields uncovered — that is, the more recent vintage covers only 40.6% of the registered fields it should cover, against 69.1% for the older one. Fragmentation differs in the same direction: the 2567 vintage places on average 1.47 polygons more than half inside each registered field against 0.53 for 2568, and the median FTW polygon in the study area is 0.60 rai (2567) or 1.14 rai (2568) against a median registered field of 13.7–15.4 rai.

Two conclusions follow, and they point in opposite directions. As a boundary product scored against contract polygons, FTW is weak: fewer than one field in ten is recovered at IoU ≥ 0.8 in either vintage. As a source of parcel geometry for fusion, it is nevertheless the strongest component available, because its errors are predominantly over-segmentation of a correct outer edge rather than misplacement of that edge — which is exactly the failure mode that a cane-fraction rule can absorb.

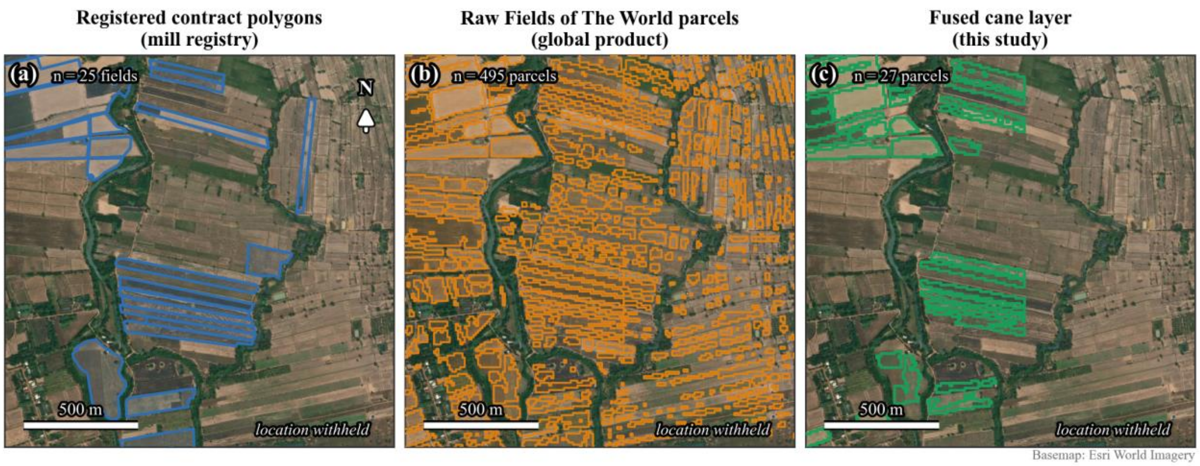

Figure 3. Parcel geometry from three sources over the same block: registered contract polygons, raw FTW parcels, and the fused cane layer. The over-fragmentation of the global product (median 0.60 rai) and its absorption by the cane-fraction rule are both visible. Scale bar only; coordinate axes removed and location withheld for confidentiality.

Table 3. Fields of The World boundaries against registered cane fields. Vintage labels follow the Thai calendar as stored in the source file. Registry and FTW geometry compared as vectors in UTM 47N.

Metric	FTW 2567 vs season 68	FTW 2568 vs season 69
Registered fields scored	1,757	1,979
FTW polygons in the same box	14,742	7,026
Median registered field size (rai)	15.37	13.74
Median best-match IoU	0.398	0.297
Best-match IoU ≥ 0.5	35.8% (33.6–38.1)	27.0% (25.1–29.0)
Best-match IoU ≥ 0.8	7.7% (6.5–9.0)	8.5% (7.4–9.9)
Median union IoU	0.493	0.295
Union IoU ≥ 0.8	9.3%	9.5%
Interior FTW polygons per field (mean)	1.47	0.53
Fields with no FTW polygon	30.9% (28.8–33.1)	59.4% (57.2–61.6)
Median FTW polygon in study area (rai)	0.60	1.14
FTW polygons in study area	2,562,127	1,834,547

4.3 The fused parcel layer

Fusing the FTW 2567 geometry with the cane classification produced 159,699 parcels whose area is at least half covered by predicted cane. Intersecting these with the registry marked 13,237 as registered and 54,014 as unregistered at the 3 rai threshold, giving a fused layer of 67,251 cane parcels covering 906,335 rai (1,450 km²) with a median parcel size of 8.01 rai (1.28 ha). The unregistered component covers 703,355 rai with a median of 7.77 rai, and the registered component 202,980 rai.

The change in the shape of the output is as important as its size. The pixel-based detector produced 23,550 patches with a strong tail of large amorphous blobs, because adjacent cane fields with no visible separation merge into one connected component; the fused layer replaces them with parcels whose median size, 8.0 rai, is within a factor of two of the median registered field, 14.8 rai, and which follow edges that are visible in imagery. The residual over-segmentation is visible in the same comparison, since the median fused parcel remains smaller than the median contract field.

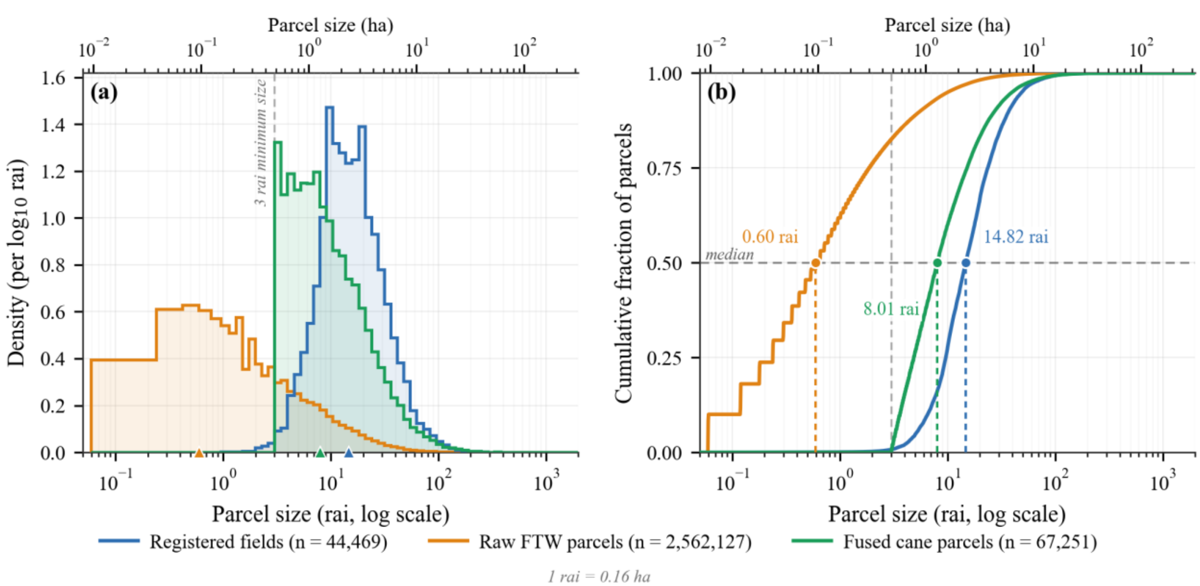

Figure 4. Parcel size distributions for registered fields, raw FTW parcels, and fused cane parcels (medians 14.8, 0.60 and 8.01 rai).

Table 4. Composition of the fused parcel layer (FTW 2567 geometry × predicted cane ≥ 50% × registry overlap ≥ 30%, parcels ≥ 3 rai).

Component	Parcels	Area (rai)	Area (km^2)	Median size (rai)
FTW parcels classified as cane (before size filter)	159,699	—	—	—
of which not matching a registration	158,919	—	—	—
Unregistered cane parcels ≥ 3 rai	54,014	703,355	1,125	7.77
Registered cane parcels ≥ 3 rai	13,237	202,980	325	—
Fused cane layer (total)	**67,251**	**906,335**	**1,450**	**8.01**

The sensitivity of these counts to both fusion thresholds is reported in Section 4.11.

4.4 Harvest-cycle evidence

Monthly NDVI over two milling seasons was used to test whether the mapped parcels behave like cane (Table 5). Of 23,550 candidate parcels covering 1,240,332 rai, 59.4% (13,996; 52.6% of area) showed a harvest-scale NDVI collapse in both seasons, 29.9% in one season only, 7.8% stayed evergreen across both seasons, and 2.9% (676 parcels, 0.5% of area) never greened at all and are therefore not cropland by this test. The two seasons agree on the harvest flag for 68.7% of parcels. Grade distribution is informative in both directions: a majority of the mapped area displays the two-season cut-and-regrow cycle that distinguishes cane from annually rotated crops, while roughly one parcel in ten falls into a class that the model is likely to have got wrong and that a field visit should target first. Median predicted probability barely varies across grades (0.849–0.883), which shows that the NDVI channel carries information the classifier does not: confidence from the embedding model is not a substitute for phenological confirmation.

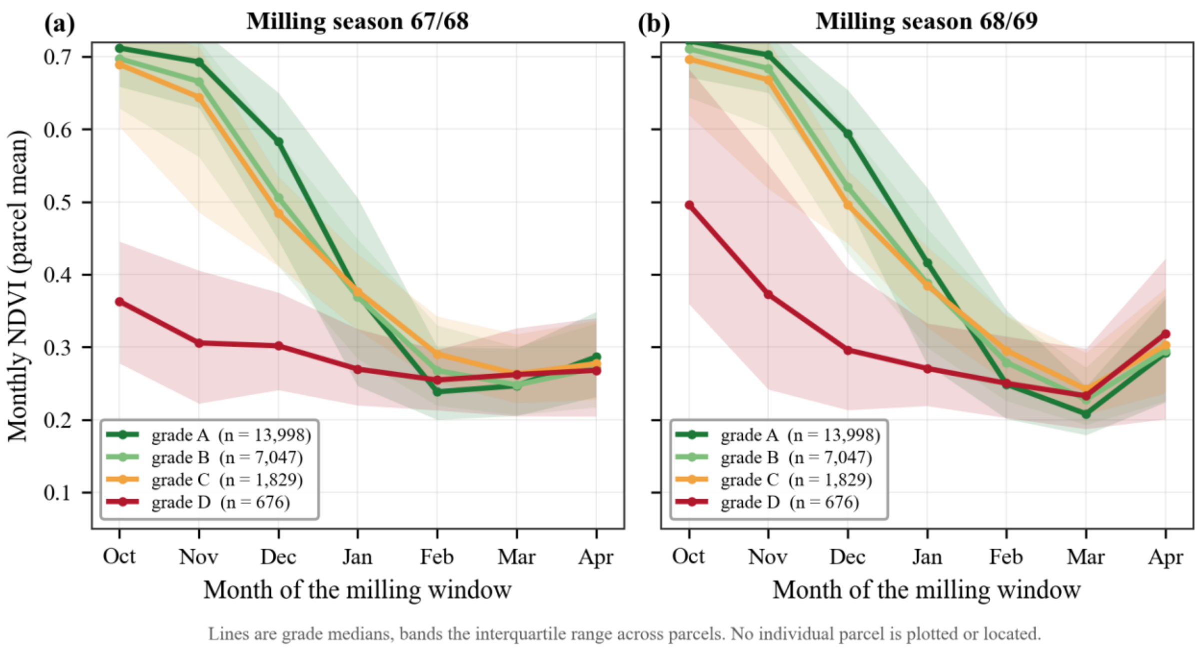

Figure 5. Monthly Sentinel-2 NDVI trajectories over two milling seasons for parcels of evidence grades A to D, showing the harvest collapse that defines grade A and its absence in grades C and D. Curves are grade medians with interquartile bands; no individual parcel is plotted or located.

Table 5. Harvest-cycle evidence grades over 23,550 candidate parcels from two milling seasons of monthly Sentinel-2 NDVI.

Grade	Definition	Parcels	% of parcels	Area (rai)	% of area	Median predicted probability
A	harvest drop in both seasons	13,996	59.4	652,360	52.6	0.871
B	harvest drop in one season	7,047	29.9	433,505	35.0	0.877
C	green but no drop in either season	1,829	7.8	147,758	11.9	0.883
D	never green (not cropland)	676	2.9	6,696	0.5	0.849
E	photograph indicates registered land	2	0.0	13	0.0	0.995

4.5 A trained boundary model does not beat the global one

The internal comparator improved monotonically across the first three configurations and then stalled well below both targets (Table 6). The best configuration, loop-4a, reached a median IoU of 0.608 on isolated holdout fields against a declared target of 0.85, and separated 21.0% of adjacent fields at IoU ≥ 0.8 against a declared target of 60% — shortfalls of 0.24 IoU and 39 percentage points. Only 18.2% of isolated fields individually reached IoU 0.85 (36/198; CI 13.4–24.1). Retraining on a larger window pool (loop-5) did not continue the trend: on its own, larger holdout the median isolated IoU was 0.561 and the separation rate 18.8%, though the evaluation universes differ between the two runs, so only the absence of a clear gain is claimed.

Across every configuration the ordering of the three decoding arms is stable and large: connected components of the interior mask collapse to a median IoU below 0.09, while both watershed arms sit near 0.55–0.61. The collapse deepened as supervision improved, from 0.136 in loop-1 to 0.076 in loop-3, and the mechanism is the label asymmetry of the task rather than a defect of the network. Unregistered cane around a registered field is spectrally identical to it but carries no polygon, so an interior head supervised over the whole window correctly reports one continuous cane region spanning the registered boundary, and connected components of that region merge whole blocks into a single instance. Boundary-guided watershed is a requirement of this task, not a refinement of it.

Placed beside Table 3, the comparator settles the design question that motivated it: a model trained on 44,469 in-domain contract polygons reaches a median IoU near 0.61 against those same contract polygons, while a zero-shot global product reaches 0.30–0.49 with no training at all and covers the catchment in one pass. The trained model is better on its own benchmark and still far from usable, which is why the production layer takes its geometry from FTW.

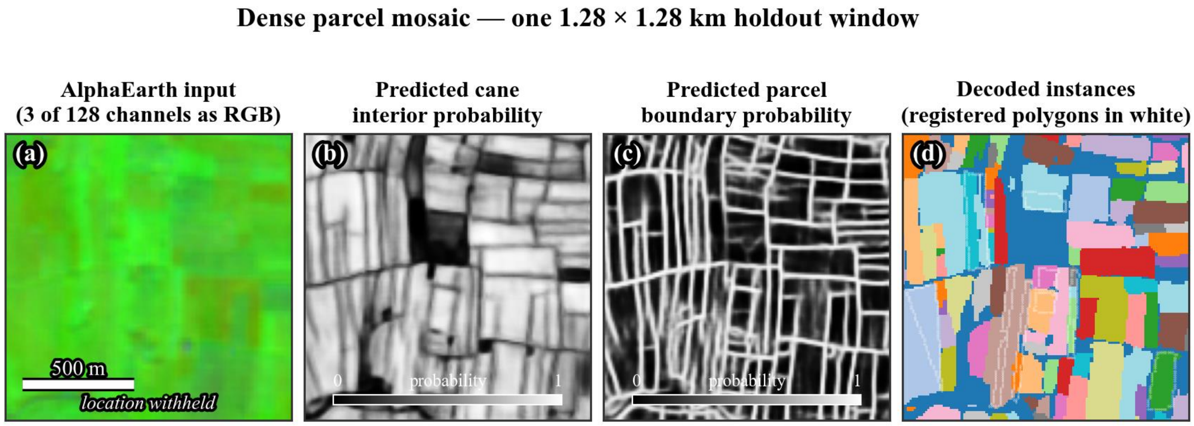

Figure 6. Trained comparator on a dense parcel mosaic. Four panels of one holdout window: three of the 128 input channels rendered as RGB; predicted cane interior probability; predicted parcel-boundary probability; decoded instances in random colours with registered polygons overlaid in white. The interior probability saturates across the whole block, which is why connected components of the interior mask merge it into a few instances (median IoU 0.08), whereas the boundary head recovers a closed lattice that the watershed can cut. Scale bar only; coordinate axes removed and location withheld for confidentiality.

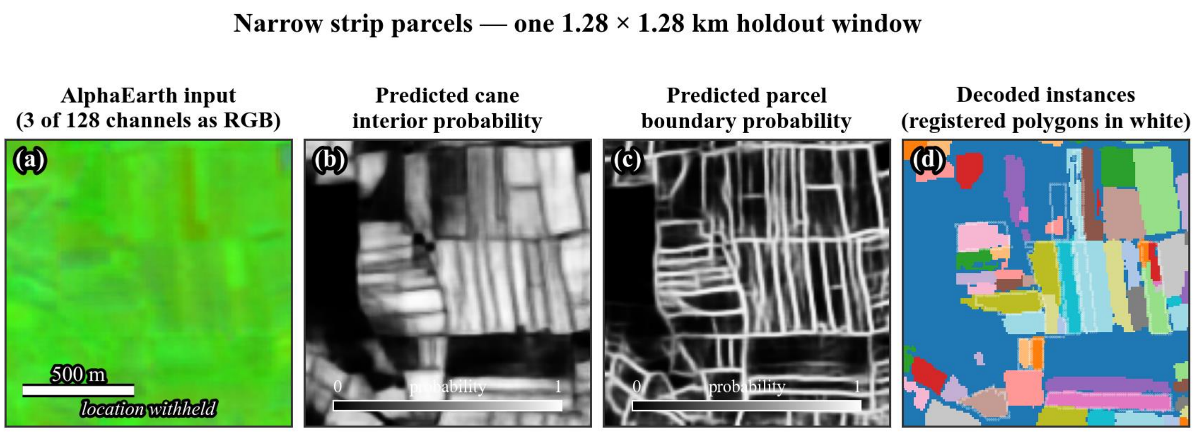

Figure 7. The same four panels for a holdout window of narrow strip parcels. Boundaries between strips a few pixels wide are resolved by the boundary head, while several neighbouring strips are still decoded as one instance, consistent with the 21.0% separation rate measured on adjacent fields. Axes removed, location withheld.

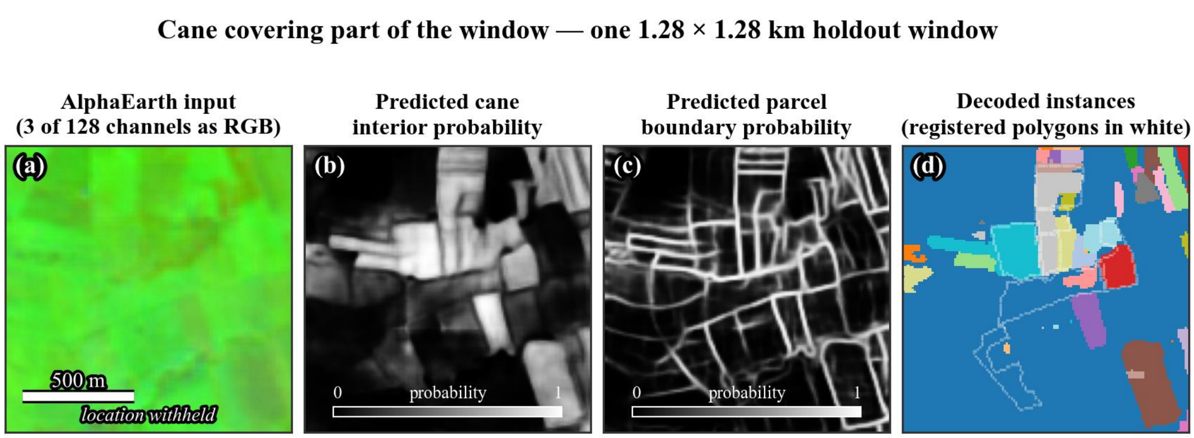

Figure 8. The same four panels where cane covers only part of the window. The interior head suppresses the non-cane land while the boundary head continues to trace field edges across it, showing that detection and delineation fail independently. Axes removed, location withheld.

Table 6. Trained detection–delineation comparator across five configurations. Boundary-constrained watershed arm unless noted; Wilson 95% CI in parentheses. Evaluation universes differ between loop-3/4a and loop-5, so the last column is read as a trend, not a controlled ablation.

Configuration / metric	loop-1	loop-3	loop-4a	loop-5
Input embeddings	64 ch, 1 year	128 ch, 2 years	128 ch, 2 years	128 ch, 2 years
Supervised fraction of window	13.8% (cores)	100%	100%	100%
Network parameters	2.00 M	4.07 M	4.07 M	4.07 M
Epochs run / best epoch	30 / 30	60 / 17	80 / —	30 / 15 (early stop)
Best selection loss	3.6889	2.0468	2.0349	2.1347
Evaluated fields (isolated / adjacent)	946 (317/629)	789 (198/591)	789 (198/591)	1,082 (341/741)
Fields dropped at window border	976	571	571	1,185
Isolated median IoU — connected components	0.1364	0.0764	0.0805	0.0841
Isolated median IoU — distance watershed	0.4831	0.5353	0.6042	0.5613
Isolated median IoU — boundary watershed	0.4966	0.5637	**0.6080**	0.5605
Isolated fields at IoU ≥ 0.85	9.1% (6.4–12.8)	14.6% (10.4–20.2)	**18.2% (13.4–24.1)**	16.4% (12.9–20.7)
Adjacent median IoU	0.4403	0.5571	0.5443	0.5304
Adjacent fields separated at IoU ≥ 0.8	14.8% (12.2–17.8)	20.3% (17.3–23.7)	**21.0% (17.9–24.4)**	18.8% (16.1–21.7)
Isolated median IoU, 24–64 px	0.662 (n=2)	0.323 (n=3)	0.590 (n=13)	0.569
Isolated median IoU, 64–160 px	0.406 (n=89)	0.532 (n=56)	0.562	0.528
Isolated median IoU, > 160 px	0.526 (n=226)	0.579 (n=139)	0.627	0.565
Training time (single run)	1,114 s	4,150 s	2,800 s	2,333 s
Declared targets	iso 0.85 · split 60%	—	**not met**	not met

4.6 Where the error lives: oracle diagnostics

Replacing components of the decoder one at a time locates the bottleneck unambiguously (Table 7). Substituting the ground-truth mask for the predicted interior mask raises the isolated median IoU from 0.608 to 1.00 and the adjacent median from 0.544 to 0.750, and more than doubles the separation rate from 21.0% to 46.2%. Substituting a per-field oracle threshold on the same predicted mask helps nothing — the isolated median falls to 0.538 and separation to 5.9% —

which shows that no single-threshold tuning of the existing probability surface can recover the gap. Morphological adjustments are similarly ineffective: dilation by one pixel leaves the medians almost unchanged while destroying separation (3.7%), and erosion by one pixel costs 0.20 IoU on isolated fields.

The systematic-bias measurements point the same way. Decoded instances are on average slightly smaller than their reference (median area ratio 0.92, median signed boundary offset −0.68 px), but that bias reverses with field size: small fields (24–64 px) are over-sized by 8% while large fields (> 160 px) are under-sized by 15%. A uniform post-hoc correction is therefore not available. What the oracle-mask result establishes is that instance decoding is not the limiting step: given a correct cane mask, the watershed already recovers isolated fields exactly and separates nearly half of adjacent ones. The residual 54% of adjacent fields that stay merged even with a perfect mask is the part attributable to contract subdivision, which no imagery can resolve.

Table 7. Oracle diagnostics on the loop-4a holdout (n = 789 fields; 198 isolated, 591 adjacent).

Decoder configuration	Isolated median IoU	Adjacent median IoU	Adjacent separated at IoU ≥ 0.8
Baseline (predicted mask, boundary watershed)	0.608	0.544	21.0% (17.9–24.4)
Oracle mask (ground-truth interior)	**1.000**	**0.750**	**46.2% (42.2–50.2)**
Oracle per-field threshold	0.538	0.433	5.9% (4.3–8.1)
Baseline dilated 1 px	0.591	0.529	3.7% (2.5–5.6)
Baseline eroded 1 px	0.412	0.405	—

4.7 Registry-conditioned decoding under the reveal protocol

Using registered polygons as walls improves the decoding of the fields that are not revealed, and the improvement survives the leakage control (Table 8). At a reveal rate of 0.5, the 283 hidden adjacent fields reached a median IoU of 0.595 against 0.530 for the same fields without walls, and their separation rate rose from 21.2% to 25.4%. At the operationally realistic rate of 0.76, the 135 hidden adjacent fields reached 0.595 against 0.544, with separation rising from 19.3% to 24.4%. Isolated fields were unaffected (0.616 against 0.617 at r = 0.5), as expected, since a wall matters only where two fields share one block. The gains are modest in absolute terms and their confidence intervals overlap, so the claim made here is directional: prior geometry helps exactly where the imagery is uninformative, and the effect size — about 4–5 percentage points of separation — bounds what registry conditioning can contribute.

A grid-consistency test in the same run doubled the decoding resolution before scoring and changed the isolated median IoU by −0.002, which indicates that the pipeline is stable to a change of grid but says nothing about sub-pixel accuracy, because the reference mask itself was rasterized at 10 m.

Table 8. Registry-conditioned decoding under the reveal protocol. Only hidden fields are scored; the baseline column is the same hidden fields decoded without walls.

Reveal rate	Hidden fields (adjacent)	Adjacent median IoU, conditioned	Adjacent median IoU, baseline	Separated ≥ 0.8, conditioned	Separated ≥ 0.8, baseline
0.50	375 (283)	0.595	0.530	25.4% (20.7–30.8)	21.2% (16.8–26.3)
0.76	185 (135)	0.595	0.544	24.4% (18.0–32.3)	19.3% (13.5–26.7)

4.8 The field-photograph channel: a negative result

Geotagged photographs from field evaluations were tested as an independent evidence channel and failed, for a structural reason that a raw count would have hidden (Table 9). At a 50 m buffer, 12,072 photographs fell on 1,812 candidate parcels, which passed the pre-set count threshold. Deduplication reduced that evidence to 4,192 distinct coordinates and 3,955 evaluations. The null model then reversed the sign of the result: photographs displaced by a random 0.5–2 km produced 15,735 hits on average (range 14,793–16,379, six replicates) against 12,072 for the real coordinates, a lift of 0.77, and under the strict rule displaced photographs produced 4,248 clean hits on average (range 3,770–4,794, eight replicates) against 120 for the real coordinates, a lift of 0.03. Real photograph positions were therefore about thirty-five times *less* likely than randomly displaced ones to land on a clean candidate.

The mechanism is structural: officers evaluate registered fields, which is the definition of their task, and registered land is excluded from the candidate set by construction, so the two distributions repel each other. Consistent with this, candidates carrying a photograph at 0 m buffer overlapped registered land in 61.3% of cases against a base rate of 0.7% over all 68,458 raw candidates, an enrichment of 87.6-fold. After removing candidates that overlap registered land and photographs that sit inside any registered polygon, 120 photographs (45 coordinates, 44 evaluations) remained on 41 candidates; requiring in addition two independent evaluations on the same candidate, an area of 1–500 rai, and a photograph more than 30 m from any registered polygon left 2 candidates covering 89.6 rai. The channel is therefore reported as a false-positive detector rather than as discovery evidence: 159 candidates covering 223,356 rai are directly contradicted by a photograph whose own registered field overlaps them.

Table 9. Field photographs joined to candidate parcels, real versus displaced coordinates.

Join	Photographs	Coordinates	Evaluations	Candidates	Lift vs null
0 m buffer	421	153	150	106	—
30 m buffer	6,876	2,432	2,310	1,059	—
50 m buffer	12,072	4,192	3,955	1,812	0.77
50 m buffer, displaced null (mean of 6)	15,735	—	—	—	—
Clean rule, 0 m buffer	120	45	44	41	0.03
Clean rule, displaced null (mean of 8)	4,248	—	—	—	—
Clean rule + 2 evaluations + 1–500 rai + > 30 m	10	—	2	2 (89.6 rai)	—

4.9 Independent cross-check against public land cover

Of 1,500 randomly sampled fused cane parcels, 98.6% (1,479; CI 97.9–99.1) fell on land whose dominant ESA WorldCover class is cropland, with a median cropland fraction of 1.00, and 1.13% (17; CI 0.7–1.8) had a dominant class of forest, grassland or built-up land and are therefore gross commission errors. The registered and unregistered components behave alike — 99.3% against 98.4% majority cropland (Table 10) — which is the more informative comparison, because the unregistered parcels are the ones with no administrative corroboration, and they are not systematically falling on non-agricultural land. This test rules out gross error only: WorldCover assigns sugarcane and cassava to the same class, and cassava is the crop that Di Tommaso et al. (2024) identify as the source of Thailand's low global F1, so a parcel can pass this check and still be cassava. It is reported because it is the one validation in this paper that a reader can reproduce from public data alone.

Table 10. Cross-check of the fused cane layer against ESA WorldCover 2021 (n = 1,500 parcels ≥ 3 rai, fixed seed). Wilson 95% confidence intervals.

Subset	n	Majority cropland	Gross error (built-up / water / tree)
All sampled parcels	1,500	98.6% (97.9–99.1)	1.13% (0.7–1.8)
Registered component	292	99.3% (97.5–99.8)	0.68% (0.2–2.5)
Unregistered component	1,208	98.4% (97.6–99.0)	1.24% (0.8–2.0)

4.10 Map accuracy

The stratified assessment of Section 3.9 has not been completed, so no overall accuracy, producer's accuracy, kappa or unbiased area estimate is reported. A separate and narrower quantity was measured: the precision of the priority list, that is the 1,000 unregistered parcels ranked highest by classifier probability and harvest evidence, which is the list an operator would act on first. The first 299 entries of that list were interpreted by an analyst against paired Sentinel-2 true-colour images of the same parcel, one from the late growing season and one from inside the milling window, without the classifier's probability or the parcel's provenance being shown.

Of 299 units, 282 were judged sugarcane, 16 were judged not sugarcane and one was undecidable, giving a precision of 0.946 (95% Wilson interval 0.915–0.967) over the 298 decisive units. Precision did not vary with parcel size: 0.953 below 10 rai (n = 190), 0.926 between 10 and 20 rai (n = 81) and 0.962 between 20 and 50 rai (n = 26).

Two limits of this number must be stated. First, it applies to the priority subset, which was filtered for shape and for a harvest signal in both milling seasons before ranking, so it is an upper bound on the precision of the full 54,014-parcel layer and not a substitute for the stratified assessment. Second, the 16 negative judgements all fall within the first 100 units: precision was 0.838 over ranks 1–100 and 1.000 over ranks 101–299. A ranked list cannot improve monotonically with rank in this way, so the pattern is more consistent with drift in the interpreter's decision threshold than with a real quality gradient, and the pooled figure should therefore be read as optimistic. The stratified sample of Section 3.9 was drawn in randomised order for exactly this reason, and completing it remains the outstanding requirement before any map-level accuracy is claimed.

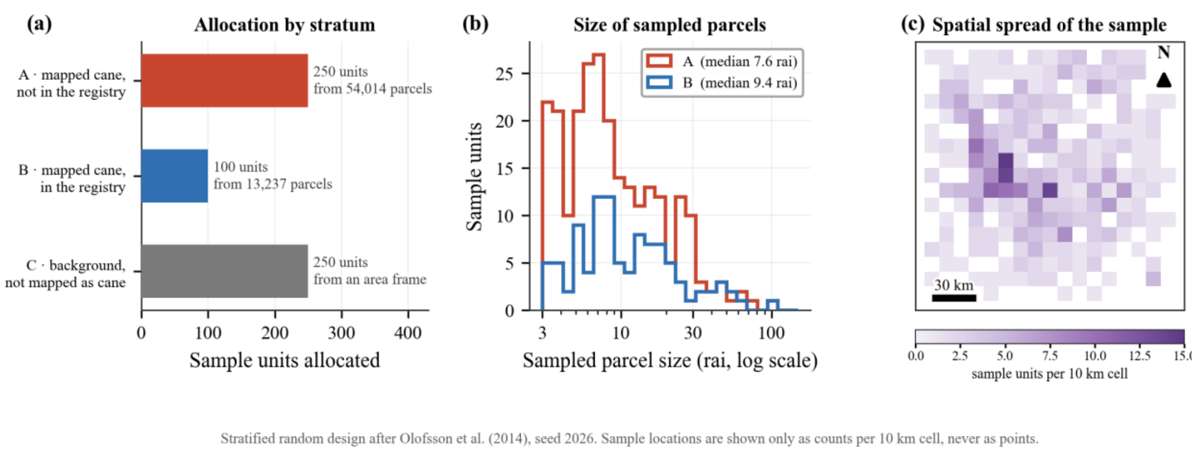

Figure 9. Design of the 600-unit stratified accuracy sample: allocation by stratum, the distribution of sampled parcel sizes, and the interpretation interface. Sample locations are shown only as counts per 10 km grid cell, never as points.

Table 11. Precision of the priority list, interpreted from paired seasonal Sentinel-2 imagery.

Subset	n	Cane	Not cane	Precision	95% CI
All decisive units	298	282	16	0.946	0.915–0.967
Ranks 1–100	99	83	16	0.838	0.753–0.898
Ranks 101–200	100	100	0	1.000	0.963–1.000
Ranks 201–299	99	99	0	1.000	0.963–1.000
Parcels < 10 rai	190	181	9	0.953	0.912–0.975
Parcels 10–20 rai	81	75	6	0.926	0.848–0.966
Parcels 20–50 rai	26	25	1	0.962	0.811–0.993

4.11 Sensitivity of the fusion thresholds

Both fusion rules of Section 3.3 — the cane-fraction threshold that admits an FTW parcel to the cane layer, and the registry-overlap threshold that separates registered from unregistered parcels — were fixed before the counts were produced, so their influence was measured afterwards over a grid far wider than either rule would plausibly be varied in practice. Overlap fractions were computed once at a floor of 0.30 and the layer was then rebuilt in memory at every combination of a cane threshold in {0.30, 0.40, 0.50, 0.60, 0.70} and a registry threshold in {0.20, 0.30, 0.40}. The count of unregistered cane parcels moved from 45,822 to 61,427 across that grid, that is between 0.85 and 1.14 times the value reported at the operating point, and mapped area moved between 0.83 and 1.17 times the reported figure (Table 12). The registry threshold was almost inert: holding the cane threshold fixed and moving the registry rule from 0.20 to 0.40 changed the parcel count by less than 1%, because parcels that overlap the registry at all tend to overlap it heavily. The median parcel size was invariant at 7.77–7.89 rai throughout, so the threshold governs how many marginal parcels enter the layer rather than what a parcel is. No conclusion in this paper depends on the exact operating point: over-fragmentation of the raw product, the size gap between mapped parcels and contract fields, and the order of magnitude of the unregistered area all hold across the full grid.

Table 12. Sensitivity of the fused layer to the two fusion thresholds. Counts are unregistered cane parcels of at least 3 rai; ratios are relative to the operating point (0.50, 0.30) used throughout the paper.

Cane threshold	Registry threshold	Parcels	Area (rai)	Median (rai)	Parcels vs operating point
0.30	0.30	61,427	821,680	7.83	1.14
0.40	0.30	57,725	760,275	7.77	1.07
0.50	0.20	53,818	694,750	7.77	1.00
0.50	0.30	54,014	703,355	7.77	1.00
0.50	0.40	54,178	711,407	7.77	1.00
0.60	0.30	50,129	644,988	7.77	0.93
0.70	0.30	45,822	582,182	7.77	0.85

5. Discussion

5.1 Why a global boundary model fragments over Thai smallholdings

FTW recovers fewer than one registered cane field in ten at IoU ≥ 0.8, and the failure is not random. The median FTW polygon in this landscape is 0.60 rai (2567 vintage) while the median registered field is 13.7–15.4 rai, a factor of more than twenty; the model is drawing structures roughly the size of a single management strip inside a field. Converting the observed agreement into an equivalent uniform boundary offset makes the magnitude concrete: for a square field of side L, a uniform boundary error d gives $\mathrm{IoU} \approx (1 - 2d/L)^2$, so the median best-match IoU of 0.398 against a median field of 15.37 rai corresponds to an equivalent offset of about 29 m, and the 2568 vintage against season 69 to about 34 m — three pixels of the input grid. Two mechanisms plausibly combine to produce this. Thai smallholder cane is planted in strips with internal access lanes and staggered ratoon ages, so a model trained to find visible discontinuities sees genuine edges that are not ownership edges; and the contract polygon is not an image object at all, so the target that the benchmark scores against is partly unobservable in principle.

The coverage difference between vintages, 69.1% against 40.6% of registered fields touched by any polygon, is the more actionable finding for practitioners, because it means that vintage selection dominates model choice: using the newer FTW file would have discarded three fields in five before any fusion rule was applied. We therefore built the fused layer on the older, denser vintage and report the newer one only as a benchmark.

5.2 The geometric ceiling at 10 m

The delineation results cannot be read without the geometry of the grid they were measured on. Rasterizing registered polygons at 10 m and scoring them against their own vector geometry gives a median IoU of 0.925 ($n = 400$), so roughly 7.5 IoU points are unreachable before any model is trained, and the penalty is carried by the perimeter and therefore falls hardest on small fields. The requirement implied by the usual IoU ≥ 0.8 criterion is stricter than it appears: by the same relation d = L(1 − √IoU)/2, reaching IoU 0.8 demands a boundary accurate to 6.7 m on a 10 rai field and 3.7 m on a 3 rai field — below one pixel of the input grid — and reaching IoU 0.85 demands 4.9 m and 2.7 m respectively. Our own comparator sits at an equivalent offset of 16.3 m on isolated holdout fields (median size 13.7 rai, median IoU 0.608) and 18.3 m on adjacent ones (12.1 rai, 0.544).

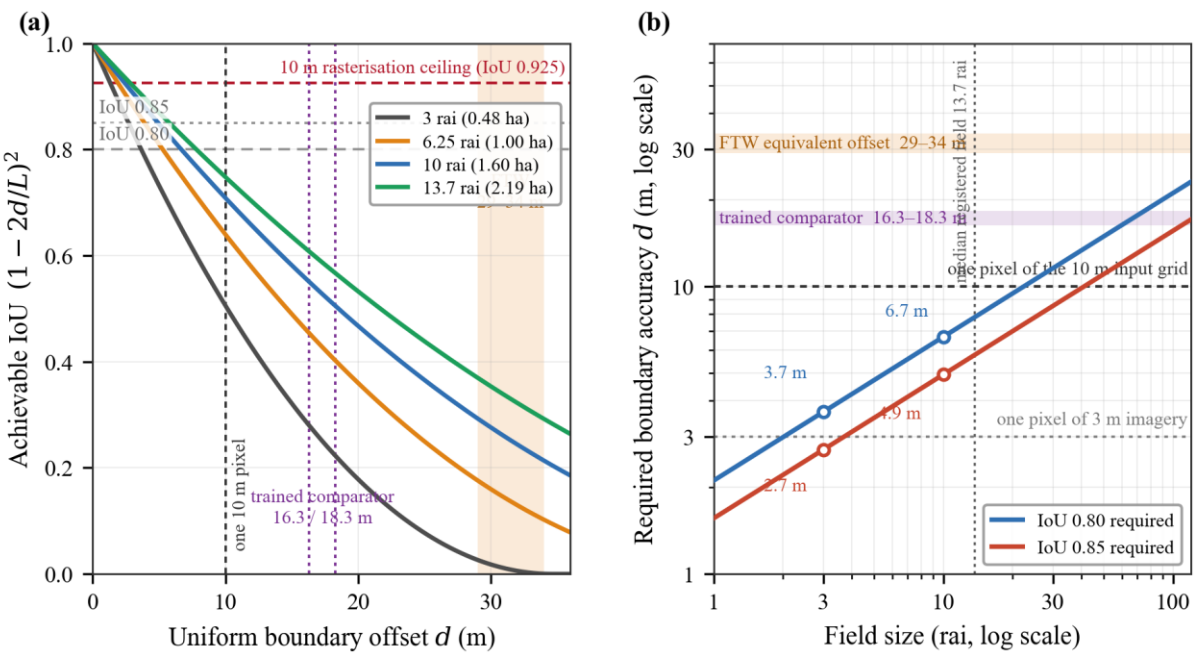

Figure 10. The geometric ceiling at 10 m. Boundary accuracy required to reach IoU 0.8 and 0.85 as a function of field size, under a uniform-offset model (d = L(1 − √IoU)/2), with the one-pixel line and the equivalent offsets measured for FTW (29–34 m) and for the trained comparator (16.3 m isolated, 18.3 m adjacent) marked.

This is where the oracle diagnostic earns its place. If the limit were the decoder, better watershed rules or a larger network would help; instead, feeding the true mask lifts isolated fields to IoU 1.00 and adjacent fields to 0.75, while an oracle threshold on the predicted mask helps not at all. The bottleneck is the mask, and the mask is limited by the grid, so the route past this ceiling is not a bigger model but a different observation: sub-pixel boundary regression, or sharper imagery for the delineation step while the embeddings continue to do the classification. That is precisely the division of labour the fused layer already adopts, with FTW playing the role of the sharper geometry.

5.3 The reference data are not a gold standard

Every IoU in this paper is measured against contract polygons, and those polygons are themselves imperfect observations of the fields they describe. Three measurements bound the problem. First, when officers photograph the field they were sent to evaluate, only 61.8% of the photographs fall inside that field's own registered polygon and 75.1% inside any registered polygon; the distance from a photograph to its own field reaches 11.1 m at the 90th percentile and 202.0 m at the 99th — the same order as the displacement that would move a photograph onto a neighbouring parcel. Second, delineation accuracy degrades monotonically with the number of neighbouring registrations while the quantization ceiling does not: over the 400 benchmark fields, the zero-shot segmentation baseline reached a median IoU of 0.666 for fields with no registered neighbour within 20 m (n = 280), 0.571 with one (n = 98) and 0.460 with two (n = 20), whereas the staircase ceiling for the same three groups is flat at 0.925 / 0.926 / 0.922. The signal being lost is ownership, not geometry. Third, 19.6% of season-68 registrations delivered no cane, so the label set contains a substantial fraction of contracts that do not correspond to a harvested field at all.

The practical consequence is that an IoU measured against this registry under-estimates true delineation quality by an unknown but non-zero amount, and that map accuracy has to be established by independent interpretation of imagery — which is why Section 3.8 exists and why no accuracy number is claimed before it completes.

5.4 Application: comparing the map with the mill registry

The most immediate application of a field-scale cane layer is to compare it with the registry, and the comparison is informative provided the ambiguity is stated. Of the 67,251 fused cane parcels, 54,014 covering 703,355 rai do not match any registered polygon. This population is heterogeneous by construction: it contains cane sold to other mills in the same provinces, cane on parcels registered in an earlier season and not renewed, model false positives on other tall row crops, and genuine gaps in the registry, and the data in hand cannot separate them. The evidence layers narrow it usefully rather than resolving it — 59.4% of candidates display the two-season harvest cycle, 2.9% are not cropland at all, and 159 candidates covering 223,356 rai are directly contradicted by a mill photograph — which converts the raw number into a prioritized work queue for field verification instead of an accusation. Reporting it any other way would over-claim: without a national parcel registry, “absent from this registry” and “unregistered” are not the same statement.

6. Limitations

First, no independent accuracy assessment exists yet. The stratified sample of 600 units described in Section 3.8 has been drawn but not interpreted, so every figure in this paper is measured against administrative records rather than against imagery interpreted by a human. Until that assessment completes, the 703,355 rai of unregistered cane is an upper bound on any registry gap and not an estimate of one, and the fused layer’s precision is unknown. The land-cover cross-check does not fill that gap: it shows that 98.6% of sampled parcels are cropland, but sugarcane and cassava share the WorldCover cropland class, and cassava is precisely the crop that depresses global cane classifiers in Thailand, so the 1.13% gross-error rate is a floor on commission error and not an estimate of it.

Second, absence from this registry does not imply illegality or even non-registration elsewhere. The catchment spans five provinces in which other mills operate, and Thailand has no central field registry that would allow a parcel to be traced to its buyer. The 89.6% detection rate on non-delivering registrations is the sharpest statement of this ambiguity we can make: nine in ten of the fields that this mill recorded as delivering nothing still look like cane to the model, and a delivery to another mill leaves no trace in these records.

Third, the geotagged-photograph channel failed as evidence, and it failed structurally rather than through poor data quality. Displaced photographs hit candidates 1.3 times more often than real ones (lift 0.77) and satisfied the clean evidence rule about thirty-five times more often (lift 0.03), because officers stand on registered fields and registered fields are excluded from the candidate set by construction. After every filter, 2 candidates covering 89.6 rai survive as positive evidence, which is not a usable channel. It is retained only as a negative control and as a false-positive detector.

Fourth, the choice of FTW vintage dominates the result and neither vintage is adequate alone. The 2568 vintage leaves 59.4% of registered fields with no polygon at all, so the production layer was built on the 2567 vintage, which still leaves 30.9% uncovered; parcels in those gaps inherit the pixel-based geometry with its blob failure mode. The fused layer is therefore not uniformly field-scale across the catchment, and the fraction that is not has not been mapped separately.

Fifth, the 10 m grid imposes a ceiling that no amount of training removes. The staircase ceiling is a median IoU of 0.925, the oracle-mask experiment shows the error is in the mask rather than in the decoder, and reaching IoU 0.8 on a 3–10 rai field requires sub-pixel boundary accuracy (3.7–

6.7 m). The trained comparator misses its pre-declared targets by 0.24 IoU and 39 percentage points, and we report it as a failed configuration rather than as a contribution.

Sixth, the delineation labels are paired with imagery from a year that is not the season's growth year. The mapping used was season 67 → 2023, 68 → 2024 and 69 → 2025, while season 68 cane was delivered between January and April 2026; because annual embeddings were published only through 2025, the alignment could not be tested, and no ablation of the season-to-year mapping was run. Any bias this introduces would apply to the comparator of Sections 4.5–4.7, not to the fused layer, whose classifier uses all three years concatenated.

Seventh, the evaluation universes are not identical across configurations, so the ablation of Table 6 is a trend and not a controlled experiment. Window generation changed between runs, 571 of 1,360 fields (42.0%) touched a window edge and were dropped in loop-3 and loop-4a and 1,185 in loop-5, and several changes were made together at each step. Within a run the three decoding arms share an evaluation set and are directly comparable; across runs, only the direction of change is claimed.

Eighth, the evidence base is one mill catchment, one imagery vintage per year, one weighbridge season, and a single round of field evaluations between 13 July and 11 August 2026. No out-of-region result is reported, no cross-season photographic check was possible, and the CCS values collected per delivery were not used in the mapping at all. Generalization to other Thai mills, to other crops, and to years in which the milling window shifts remains untested.

Ninth, the reference data cannot be released, which limits what an external reviewer can verify directly. All four inputs to the map are public and the processing chain is reproducible anywhere, but the registry, weighbridge and photograph records that supply the labels and most of the validation in this paper are confidential mill property and are withheld together with all per-parcel geometry and coordinates. Independent replication of the specific numbers reported here therefore requires a comparable local reference set; what is offered instead is a fully specified method, public inputs, and a validation protocol (Section 3.8) that any group can run on their own catchment.

7. Conclusions

A field-scale sugarcane map for a Thai mill catchment can be built today from public data by letting each component do only what it is good at: annual satellite embeddings decide whether a pixel is cane, a global boundary model supplies the parcel geometry that a per-pixel classifier cannot, and administrative records decide what the parcels mean. The fused layer resolves 67,251 cane parcels with a median size of 8.0 rai, against 0.6 rai for raw global boundaries and 23,550 amorphous patches for the classifier alone. Two findings may generalize beyond this catchment: the global boundary product over-fragments smallholder cane by more than an order of magnitude in parcel size and varies by a factor of two in coverage between vintages, so vintage selection matters more than model choice; and the residual delineation error lies in the cane mask rather than in the instance decoder, since an oracle mask raises isolated-field IoU from 0.61 to 1.00. The remaining requirement is the one that no amount of modelling substitutes for — an independent, human-labelled accuracy assessment, which is in progress and which will determine what the map can be used for.

Data and code availability

Every input needed to build the map is public. The AlphaEarth Satellite Embedding dataset is freely available (produced by Google and Google DeepMind, CC-BY 4.0); the Fields of The World global field-boundary predictions for Thailand are public (CC-BY) and were read directly from the published parquet distribution; Sentinel-2 L2A data are public through the Copernicus programme and were accessed through the AWS Earth Search and Microsoft Planetary Computer STAC catalogues; and ESA WorldCover v200 is public (CC-BY). A reader with no access to any private dataset can therefore reproduce the full processing chain — embedding features, positive-unlabelled classification, parcel fusion, harvest-cycle evidence, and the land-cover cross-check — over their own area of interest; what they would need to supply is a local reference set for calibration and validation, of the kind described in Section 3.8.

The reference data are confidential and are not released. The registered field polygons (44,469 field-seasons), the weighbridge delivery and CCS records (74,516 deliveries), and the field-evaluation photographs are commercially confidential property of the mill group, contain personal data protected under Thailand's PDPA, and cannot be redistributed in any form, including as derived per-parcel geometry, coordinates or identifiers. No raw record, no per-parcel coordinate and no map of individual parcels is provided as supplementary material; supplementary tables are restricted to the aggregate statistics already reported in this paper. Requests for access to the underlying records are a matter for the data owner.

Processing code and the parameter values used at every step (feature construction, the two-step positive-unlabelled classifier and its spy calibration, the fusion thresholds, the Sentinel-2 harvest kernel, the delineation model and decoding arms, the evaluation protocols, and the accuracy-assessment sampler and scorer) are available from the authors on reasonable request, excluding model weights trained on confidential polygons.

Institutional Review Board Statement

Not applicable. This study analysed satellite imagery and de-identified agronomic records; it involved no human participants and no animal subjects.

Informed Consent Statement

Not applicable. No individually identifiable personal data were used; all grower-identifying attributes were removed before analysis and all results are reported as aggregates.

Ethics and confidentiality

Grower data were accessed and processed under an agreement with the mill group that owns them and were used solely for the research reported here. No personal data are disclosed: grower names, contract identifiers, quota codes and per-parcel coordinates were removed before analysis and appear in no table, figure, appendix or supplementary file. All results are reported as aggregate statistics, and all map products in this paper are generalized — spatial distributions are shown as gridded densities and example scenes are shown without coordinate axes — so that no individual field or grower can be located or identified from the published material. This treatment follows Thailand's Personal Data Protection Act (PDPA) and the terms of the data agreement. The study makes no statement about the legal status of any parcel: as set out in Sections 1 and 5.4, absence from one mill's registry is not evidence of unregistered or unlawful cultivation, and the results are framed as a prioritized list for field verification rather than as findings about any grower.

Generative AI disclosure

Generative AI assistance (Anthropic Claude models, accessed through the Claude Code command-line interface) was used during this work to write and review analysis code, to orchestrate experiment runs, and to draft and edit the text of this manuscript. All experimental designs, thresholds and targets were fixed by the authors before the corresponding runs; every numerical value reported here was produced by the released code from the stated data sources and was checked by the authors against the run outputs; no data, results, references, or citations were generated by an AI system. The authors take full responsibility for the content of the manuscript.

Author contributions, funding and competing interests

Watcharapon Thod is the sole author and is responsible for all parts of this work under the CRediT taxonomy: conceptualisation, methodology, software, formal analysis, data curation, validation, visualisation, writing of the original draft, and review and editing.

No external funding was received for this study. All satellite inputs used to build the map — the AlphaEarth Satellite Embedding dataset, the Fields of The World global boundary product, Sentinel-2 Level-2A imagery and ESA WorldCover — are publicly available at no cost. Computation was carried out on freely available cloud notebook resources.

The author declares no competing financial or non-financial interests. The reference datasets were made available by a commercial sugar mill under a confidentiality agreement; the mill had no role in the design of the analysis, in the interpretation of the results, or in the decision to publish.

Author biography

Watcharapon Thod is a full-stack AI engineer with a background in computer science at Kasetsart University. His work applies machine learning to agricultural remote sensing, with a focus on field-scale crop mapping, geospatial foundation models, and the use of operational agro-industrial records as reference data for satellite-derived products.

References

Beucher, S., Meyer, F. (1993). The morphological approach to segmentation: the watershed transform (Beucher & Meyer, 1993)ation. In: *Mathematical Morphology in Image Processing*, Marcel Dekker, 433–481.

Bekker, J., Davis, J. (2020). Learning from positive and unlabeled data: a survey. *Machine Learning*, 109, 719–760.

Brown, C.F., et al. (2025). AlphaEarth Foundations: an embedding field model for accurate and efficient global mapping from sparse label data. *arXiv:2507.22291*.

Di Tommaso, S., et al. (2024). Global sugarcane mapping from Sentinel-2 imagery. *Earth System Science Data*, 16, 4931–4947.

Elkan, C., Noto, K. (2008). Learning classifiers from only positive and unlabeled data. In: *Proceedings of the 14th ACM SIGKDD International Conference on Knowledge Discovery and Data Mining*, 213–220.

Ke, G., Meng, Q., Finley, T., Wang, T., Chen, W., Ma, W., Ye, Q., Liu, T.-Y. (2017). LightGBM: a highly efficient gradient boosting decision tree. In: *Advances in Neural Information Processing Systems*, 30, 3146–3154.

Kerner, H., et al. (2024). Fields of The World: a machine learning benchmark dataset for global field boundary segmentation. *arXiv:2409.16252*.

Kirillov, A., et al. (2023). Segment Anything. *arXiv:2304.02643*.

Liu, B., Lee, W.S., Yu, P.S., Li, X. (2002). Partially supervised classification of text documents. In: *Proceedings of the 19th International Conference on Machine Learning*, 387–394.

Olofsson, P., Foody, G.M., Herold, M., Stehman, S.V., Woodcock, C.E., Wulder, M.A. (2014). Good practices for estimating area and assessing accuracy of land change. *Remote Sensing of Environment*, 148, 42–57.

Poortinga, A., et al. (2021). Mapping sugarcane in Thailand using transfer learning, a lightweight convolutional neural network, NICFI high-resolution satellite imagery and Google Earth Engine. *ISPRS Open Journal of Photogrammetry and Remote Sensing*, 1, 100003.

Ronneberger, O., Fischer, P., Brox, T. (2015). U-Net: convolutional networks for biomedical image segmentation. In: *Medical Image Computing and Computer-Assisted Intervention (MICCAI)*, 234–241.

Suwanlee, S.R., et al. (2025). Mapping sugarcane plantations in Northeast Thailand using multi-temporal data from multi-sensors and machine-learning algorithms. *Big Earth Data*, 9(2), 187–216.

Appendix A. Verification steps

These figures are the working checks carried out while the layer was being built. They are reproduced here because each one tests a different claim made in the body of the paper, and because several of them are the reason a design decision was taken. As everywhere else in this paper, no coordinate axis, coordinate list or place name below province level is shown; every panel is a location-withheld extract.

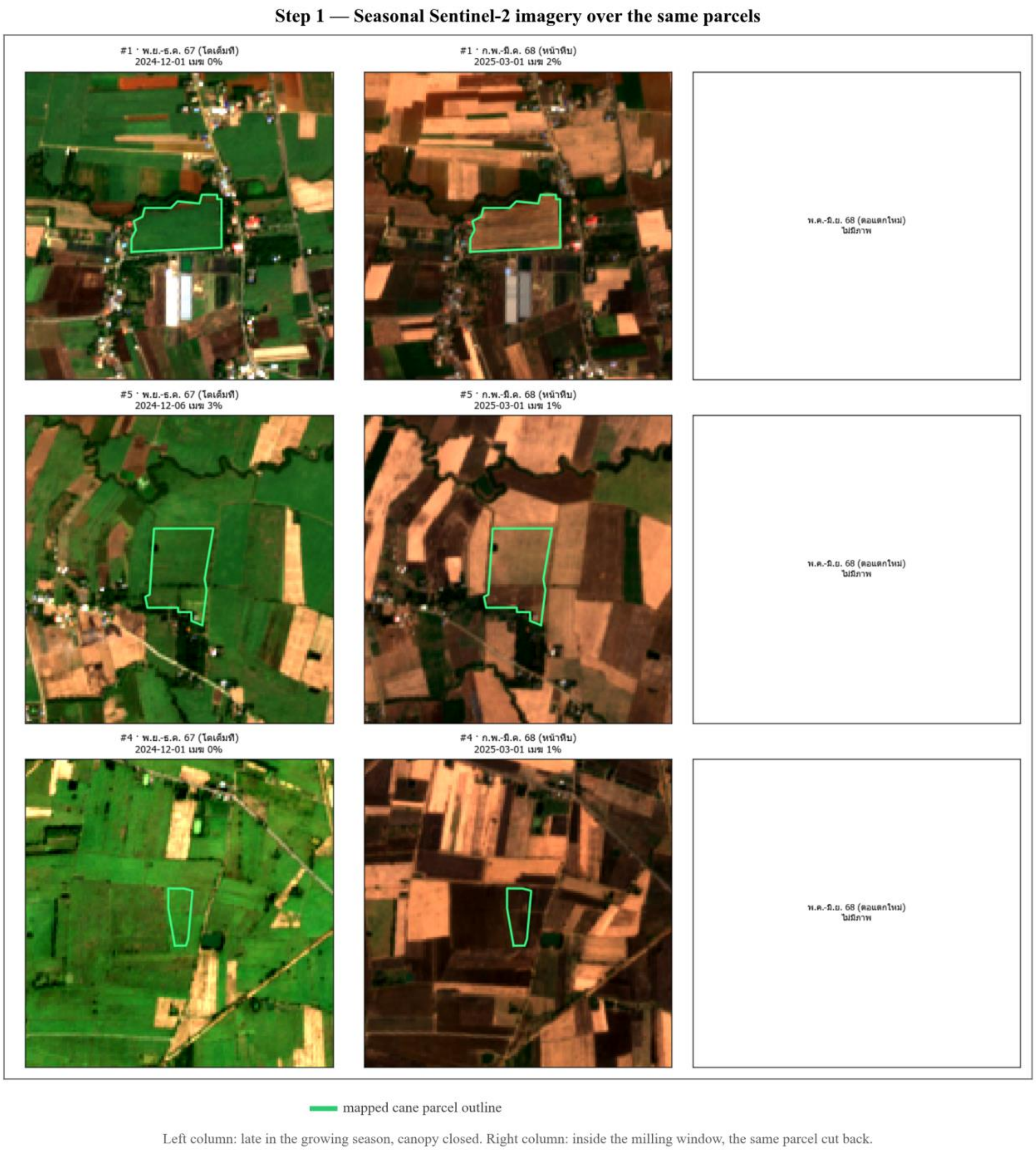

Figure A1. Seasonal Sentinel-2 imagery over the same mapped parcels, late in the growing season (left) and inside the milling window (right).

What it establishes: that the parcels the map calls cane actually follow the cane calendar. The same outline carries a closed canopy before the milling window and bare or stubble ground inside it. This is the visual counterpart of the NDVI harvest-drop test in Section 4.4: a parcel that never changes between these two dates cannot be cane being cut for delivery, and would fall into grade C or D.

Figure A2. Nine mapped parcels drawn on high-resolution basemap imagery, with parcel size in rai and predicted cane probability in each header.

What it establishes: that the mapped outlines land on real, coherent field objects rather than on classifier noise, across a range of sizes and shapes — from compact blocks to long strips. It also shows the failure mode the delineation sections quantify: the outline is placed on the right field, but its edge can be one to two pixels off, which is what limits IoU at 10 m (Section 5.2).

Figure A3. Parcel edges before fusion (pixel-detector patches) and after fusion with Fields of The World geometry, over the same six blocks.

What it establishes: the change in the shape of the output reported in Section 4.3. Before fusion the detector produces amorphous patches that merge adjacent fields with no visible separation; after fusion the same area is carried by parcels whose edges follow discontinuities that are visible in the imagery. This is the evidence that fusion changes the geometry of the product, not merely its area.

Figure A4. Three sources of parcel geometry over the same blocks: the global field-boundary product, the mill registry, and the boundaries produced by the model trained here.

What it establishes: the two findings of Section 4.2 and Table 3 in visual form. First, the global product subdivides a single contract field into management strips — the over-fragmentation that gives a median FTW polygon of 0.60 rai against a median registered field of 13.7–15.4 rai. Second, the registry polygon is a contract, not an image object, so part of the disagreement between the two is unobservable in principle and cannot be fixed by a better model.

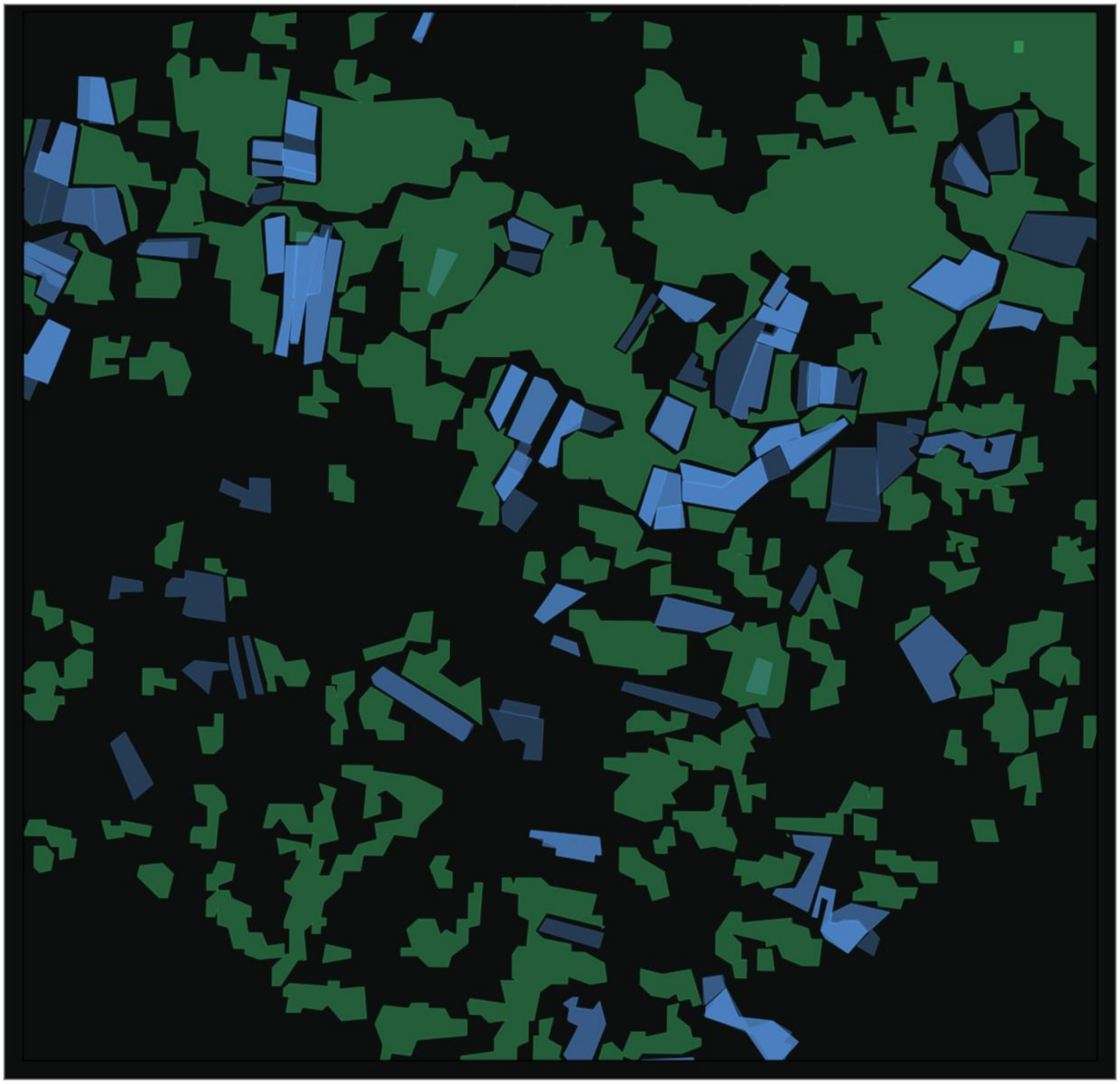

Figure A5. Block-level check at about 4 km across: unregistered cane found by the model against registered contract polygons.

What it establishes: that the unregistered class is not a re-detection of registered land. The two layers interlock and fill different ground; if the model were simply firing again on the fields it was trained on, the green and blue areas would coincide instead of tessellating.

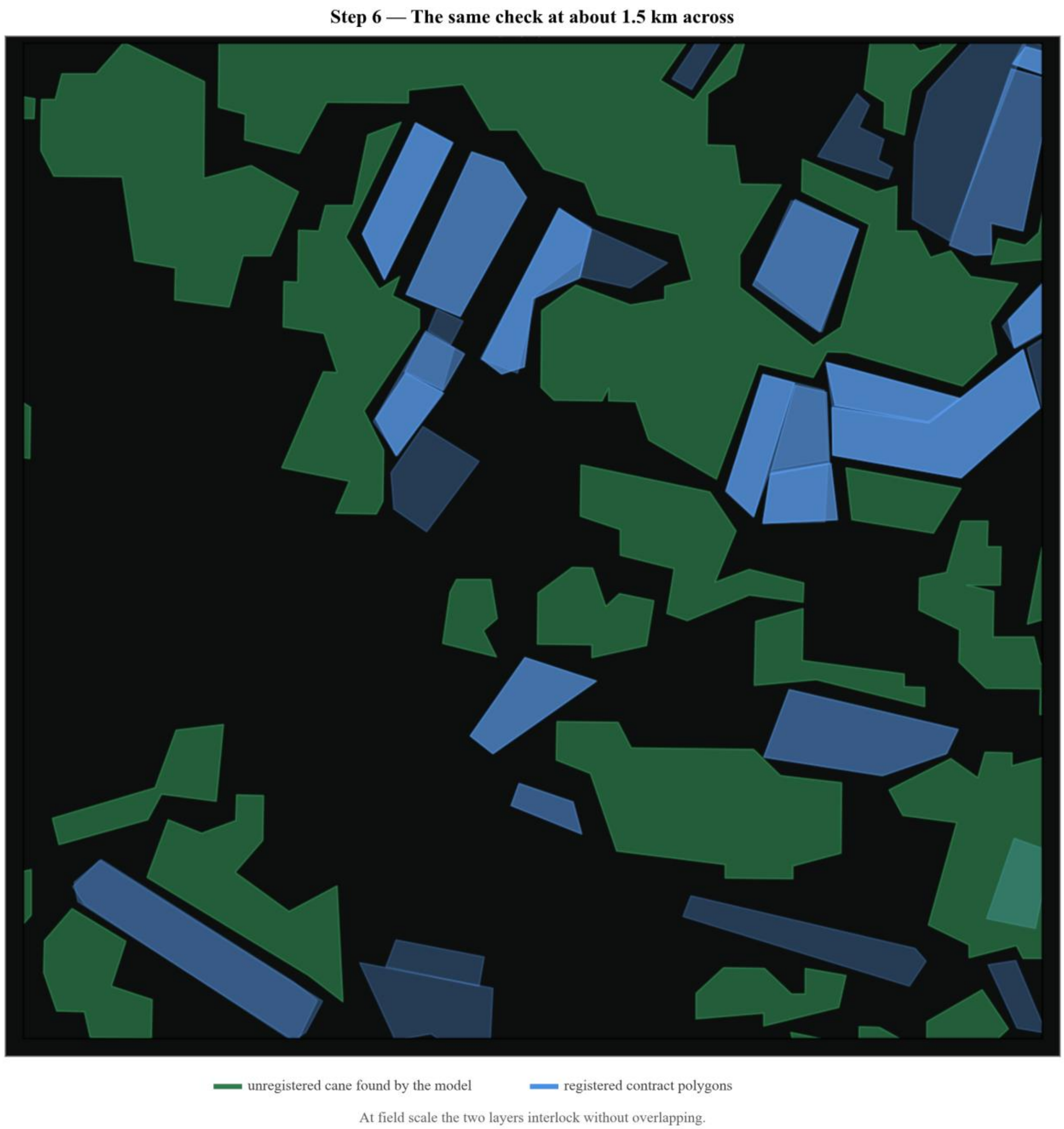

Figure A6. The same check at about 1.5 km across.

What it establishes: the same conclusion at field scale, where individual parcel edges are resolvable. It also shows the residual over-segmentation acknowledged in Section 4.3 — a single physical field is sometimes carried by two adjacent mapped parcels, which is why the median fused parcel (8.01 rai) stays smaller than the median contract field.